

Preparation of activated red mud particle adsorbent and its adsorption mechanism for phosphate ions

Longjiang Li^{a,b,c,d}, Qin Zhang^{b,c,d,*}, Xianbo Li^{b,c,d}, Wei Cheng^{b,c,d}, Lan Ban^{b,c,d}

^aCollege of Metallurgy and Materials Engineering of Guizhou University, Guiyang 550025, China, Tel. +86-851-88292081; email: qzhang@gzu.edu.cn (Q. Zhang), Tel. +86-851-83627268; email: 750119957@qq.com (L. Li)

^bMining College of Guizhou University, Guiyang 550025, China, email: xbli1990@163.com (X. Li)

^cNational & Local Joint Laboratory of Engineering for Effective Utilization of Regional Mineral Resources from Karst Areas, Guiyang 550025, China, email: wcheng1983@126.com (W. Cheng)

^dGuizhou Key Laboratory of Comprehensive Utilization of Non-metallic Mineral Resources, Guiyang 550025, China, email: 841471916@qq.com (L. Ban)

Received 6 February 2019; Accepted 13 December 2019

ABSTRACT

Herein, granulation molding was conducted using a disc granulator via a two-step rolling granulation method. Red mud (RM), which has good absorption efficiency on phosphate ions in wastewater, was used as the raw material, and some amount of fly ash was doped as a pore-assisting modifier. High belite cement and hydroxypropyl methyl cellulose were used as binders; HCl was the active modifier, and H₂O₂ and MnO₂ were the pore regulators. A non-thermally activated red mud particle adsorbent (ARMFA) was prepared via an optimal formulation of the above additives, and the adsorbent had 9.25 pH, 40.54 m² g⁻¹ specific surface area, 2.10 cm³ g⁻¹ pore volume, 1.31 KPa compressive strength, and 3.72% pulverization rate at 24 h. This adsorbent can be used to adsorb phosphate ions (P) in phosphate ore dressing plant discharge wastewater. For 156.7 mg L⁻¹ total initial P concentration, 25 g L⁻¹ ARMFA amount, 14 h adsorption time, and 38.46 mg g⁻¹ adsorption and 98.17% removal rate of the total P were achieved. Particularly, the toxicity of ARMFA was below the standard limit. When the pH was 8–9, P mainly existed in the form of HPO₄²⁻ and PO₄³⁻. These ions reacted with Ca²⁺, Na⁺, Al³⁺, Mg²⁺, etc., and formed strong chemical bonds through surface deposition and ion exchange, which were then distributed on the inner surface of the ARMFA channels. The adsorption of P by the ARMFA is per the pseudo-second-order dynamics model, and the Langmuir model can best describe the adsorption process. Phosphorus, fluorine, and other toxicity indicators in the tailwater after adsorption reached the standard requirements. After adsorbing P, the alkalinity of the ARMFA decreased, and the metal ions and toxic substances were consolidated. These results provide a foundation for the use of RM in building materials.

Keywords: Non thermally activated red mud particle adsorbent (ARMFA); Phosphate ion; Phosphate flotation tailwater; Adsorption mechanism

1. Introduction

The percolating water (PW) from a phosphate ore flotation tailings reservoir comprises the phosphate ore flotation wastewater leached from the bottom of the tailings dam via

dilution with rainwater and percolation of phosphate rock tailings or soil [1]. The diversity of phosphate rock properties determines the complexity of phosphate ore beneficiation wastewater. In general, pH, chemical oxygen demand, biological oxygen demand (BOD), solid suspension (SS), P, S,

* Corresponding author.

F, and other indicators in phosphate rock flotation wastewater exceed the National Discharge Standard Rank 2 in China for industrial wastewater [2]. Discharging this kind of wastewater directly into a water body will change the pH value of the water body and hinder its self-purification, inhibit the growth of bacteria and microorganisms, and destroy the normal ecological cycle [3]. More specifically, the total phosphorus content of this type of PW can reach as high as ~50–150 mg L⁻¹. Therefore, it must meet national standards before it can be discharged; otherwise, it will lead to eutrophication of water bodies [4].

At present, wastewater treatment methods primarily include solidification, froth flotation, filtration, ion exchange, aerobic and anaerobic treatment, advanced oxidation treatment, solvent extraction, adsorption [5,6], electrolysis, microbial reduction, and activated sludge [7]. However, these technologies must be further improved due to their insufficient removal of pollutants, high cost, and high requirements for reagents and/or energy consumption. In addition, some may produce toxic residues or other wastes that require further safe disposal [8]. The removal of contaminants from water through adsorption is considered the most versatile treatment method. Activated carbon is a promising adsorbent that is commonly used to remove different types of contaminants from water and wastewater. However, the widespread use of activated carbon in water treatments is limited by its high cost. Therefore, the development of low-cost adsorbent materials has become the main focus in this field [9,10].

Red mud (RM) is the red muddy solid waste remaining after the extraction of the Al₂O₃ component from bauxite in the aluminum industry production process [11,12]. As the surfaces of calcium, sodium, aluminum, and magnesium oxides in RM have a strong reactivity, RM demonstrates good adsorption to heavy metal ions [13] such as Cu²⁺, Pb²⁺, Zn²⁺, Ni²⁺, Cr²⁺, and Cd²⁺ in water [14,15]. It contains a large number of metal oxides and silicates that can form a structure with a certain functional group on the surface and remove specific anions through ligand exchange and surface precipitation [16]. Many scholars have observed that both original and modified RM exhibits certain removal characteristics for anionic pollutants (AsO₄³⁻, AsO₃³⁻, F⁻, PO₄³⁻) in water [17]. RM can effectively remove phosphate ions from water [18]. More specifically, CaO, Al₂O₃, and Fe₂O₃ can form insoluble precipitates with phosphate, while Al₂O₃ can also undergo hydroxylation at a certain pH value and adsorb and coagulate the phosphorus in water [19]. The iron, aluminum, and silicon oxides on the RM surface can be hydrolyzed in water. Thus, the adsorption of phosphorus can be explained by the ligand exchange reaction mechanism.

A lot of research has been conducted to improve the adsorption capacity of RM to phosphate. In summary, it can be divided into shape regulation (powder, columnar, granular, flake), acid activation (hydrochloric acid, sulfuric acid, nitric acid, carbon dioxide) [20], calcination activation (control of sintering temperature) [21], combined activation technology, and static, dynamic adsorption, and desorption control techniques as well as related mechanism research work. These works have laid a good foundation for the application of phosphate ion removal via RM from phosphorus-containing wastewater.

However, RM as an alternative to activated carbon does not have a large-scale adsorbent application for phosphorus-containing wastewater, and there are still some limitations in the current research. Firstly, the phosphorus-containing wastewater used in most studies is a simulated phosphorus-containing liquid that has a certain guiding significance for the mechanism discussion; however, the composition of actual industrial wastewater is more complicated, so it is necessary to evaluate the adsorption capacity of RM to multi-component pollutants. Secondly, adsorbents prepared via the calcination method have excellent adsorption performance and their waterproof erosion meets the requirements, but their roasting cost is too high. However, powder or particulate adsorbents prepared via a non-calcination method do not consider the relationship between porosity and particle compressive shear resistance, resulting in a lower adsorption efficiency. Thirdly, the acid activation needs to be immersed in a large amount of acid solution and then dried. Acid decomposition in the filtration and drying processes causes secondary pollution to the water and air and is also of the high cost. Finally, the shape control of the pores of the adsorbent is neglected, and an efficient semi-open pore adsorption mode is not formed.

Therefore, this study aimed to improve the anti-powdering performance, adsorption performance, and strength of the RM particle adsorbent and reduce production costs and environmental pollution. RM is used as the raw material, and fly ash (FA) (pore-assisting agent), C₂S-HPMC (hydroxy propyl methyl cellulose) (binders), HCl (modified active agent), and H₂O₂-MnO₂ (pore-forming active agents) are added to prepare a non-thermally activated red mud particle adsorbent (ARMFA) through a two-step granulation method. This product is environment-friendly and has a high porosity, strong adsorption capacity, strong powder resistance, and good mechanical properties. In this paper, the adsorption of the phosphate ions (total P) in the PW of the tailings dam of the Guizhou WengFu Phosphorus Ore Dressing Plant, (Guizhou Province, China) by the experimentally prepared ARMFA is discussed, and the adsorption mechanism of ARMFA to P is revealed, laying a foundation for its large-scale industrial application.

Overall, the properties of the modified RM are improved after adsorption of the total P. Firstly, high-aluminum cement curing agent and FA are introduced in the process of modification, curing most heavy metal ions in the RM itself and increasing the active component (Al₂O₃). Secondly, when the RM absorbs the total P, its pH value and influence on the environment decrease; this could promote its mass use in building materials. Thirdly, phosphate material is formed after the adsorption, making the RM system more stable [22]. From the perspective of material applications, RM soaked in phosphorus tailwater could be used as an admixture of concrete with better mechanical properties that could reduce the anti-alkali phenomenon of materials added with RM. It could be used for concrete strength excitation and in particle fillers or soil improvers. Therefore, after the adsorption of phosphate material, it is equivalent to using phosphoric acid tailwater to comprehensively modify alkaline RM to achieve the purpose of treating waste with waste.

2. Materials and methods

2.1. Raw materials and reagents

The RM sample was collected from Guizhou HuaJin Aluminum Co. Ltd., (Guizhou Province, China), with a water content of 30%. After being dried at 50°C for 12 h, it was ground by a planetary ball mill through a 0.074 mm mesh sieve. The X-ray diffraction (XRD) pattern is shown in Fig. 1. The main minerals found were red iron (Fe_2O_3), calcium aluminum oxide hydrate ($\text{CaAl}_2\text{O}_4 \cdot 10\text{H}_2\text{O}$), katoite ($\text{Ca}_3\text{A}_{12}(\text{OH})_{12}$), cancrinite ($\text{Na}_6\text{Ca}_{1.5}\text{Al}_6\text{Si}_6\text{O}_{24}(\text{CO}_3)_2 \cdot \text{H}_2\text{O}$), anhydrite (CaSO_4), calcium phosphate silicate ($\text{Ca}_2\text{SiO}_4 \cdot 0.05\text{Ca}_3(\text{PO}_4)_2$), tilleyite ($\text{Ca}_3\text{Si}_2\text{O}_7(\text{CO}_3)_2$), calcium zinc aluminum oxide ($\text{Ca}_3\text{Al}_4\text{ZnO}_{10}$), and calcite (CaCO_3). The FA sample was collected from Qiantong Fly Ash Co. Ltd., Fuquan City, Guizhou Province, China. The original ash had a loss on ignition of $\leq 5\%$, SiO_2 content $\geq 30\%$, and SO_3 content $\leq 2\%$; it was secondary FA and the ground to less than 200 mesh before use. The XRD pattern is shown in Fig. 2. The main minerals observed included quartz (SiO_2), magnesite (MgCO_3), rostitite ($\text{Al}(\text{SO}_4)(\text{OH}) \cdot 5\text{H}_2\text{O}$), calcium aluminum oxide ($\text{Ca}_3\text{Al}_2\text{O}_6$), and tricalcium aluminate ($\text{Ca}_3\text{Al}_2\text{O}_6$).

Thermogravimetric analysis was performed on the RM material, as shown in Fig. 3. The weight loss curve of the RM was divided into three stages. The temperature ranged from 25°C to 247.7°C for the surface adsorption water volatilization stage, in which free water and surface adhesion water were lost. The temperature from 247.7°C to approximately 534.3°C was the removal stage of internal crystalline and combined water. The weight of the water removed by the two parts accounted for about 7.5%. The decomposition stage of organic carbonation and carbonate occurred when the temperature ranged from 534.3°C to 713.2°C. Therefore, the weight loss rate was relatively fast. After the temperature rises above 713.2°C, the weight loss tended to be gentle. When the temperature reached 897.7°C, the weight essentially did not change. The 7.5% moisture content of the RM had to be considered in the parameter conditions when preparing the RM particle adsorbent.

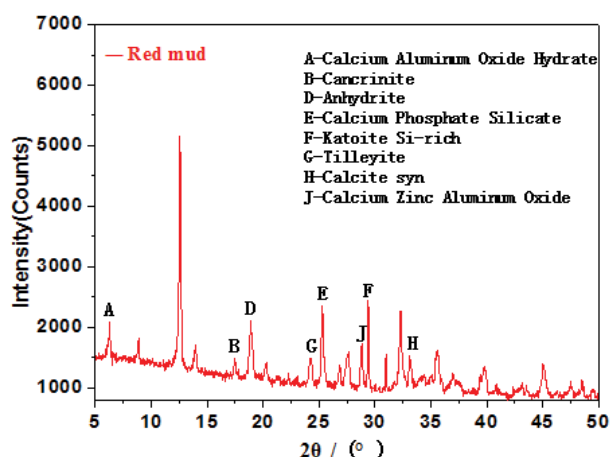


Fig. 1. XRD pattern of the RM.

The composition analysis results of the PW are shown in Table 1. The total P content was 156.7 mg L^{-1} , which exceeded the GB3838-02 National Industrial Wastewater Discharge Standard Rank 2 (in which the emission standard of total P must be less than 0.5 mg L^{-1}), so it could not be directly discharged without treatment.

The cement used was 42.5R C_2S , purchased from Tangshan Polar Bear Building Materials Co. Ltd., (HeBei Province, China). Moreover, H_2O_2 (industrial grade, 30%) was purchased from Tianjin Hongshuoda Trading Co. Ltd., (Tianjin Province, China); MnO_2 (industrial grade) from Chengdu Jinshan Chemical Reagent Co. Ltd., (Chengdu Province, China); HPMC (industrial grade, 2 million sticks) from Hebei Yanxing Chemical Co. Ltd., (Hebei Province, China); HCl (concentration 36%–38%, analytical grade) from Hengyang Guangheng Hongda Chemical Co. Ltd., (China); and HCl (concentration 38%, analytical grade) from Guangzhou Wan Cong Chemical Co. Ltd., (Guangzhou Province, China). Standard Ca, Mg, Si, P, Al, and Fe solutions were developed by the Beijing Research Institute of Nonferrous Metals, (Beijing Province, China); HNO_3 (analytical grade, 68%) was purchased from Guangzhou Wancon Chemical Co. Ltd., (Guangzhou Province, China), and deionized H_2O was self-prepared in the laboratory.

2.2. ARMFA particle adsorbent preparation

2.2.1. Preparation scheme

It has been found that when the size of adsorbent particles is larger than 2 mm, it is difficult for the solution to penetrate into the center of the ball in a short time, thereby prolonging the adsorption time. In addition, if there is no supporting core, the strength of the adsorbent particles will be low and the dynamic adsorption loss rate will be relatively high. In the pore-making process, the pores can easily become through-holes. Moreover, it is not good for adsorption if the pores are worn along the latitude and longitude lines. Therefore, in this study, the granulation design was performed first during the granulation process. The ARMFA model is shown in Fig. 4. The adsorbent particle had

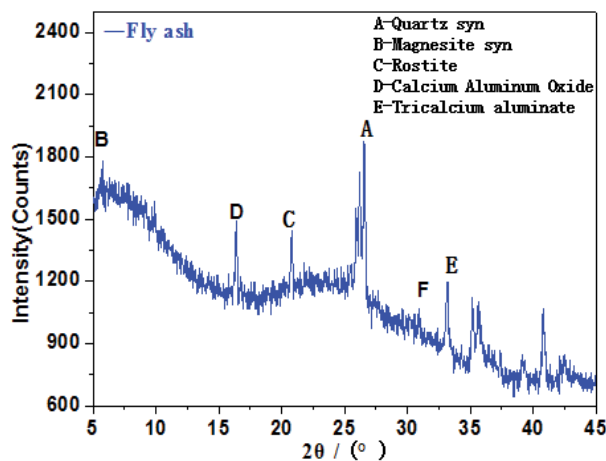


Fig. 2. XRD pattern of the FA.

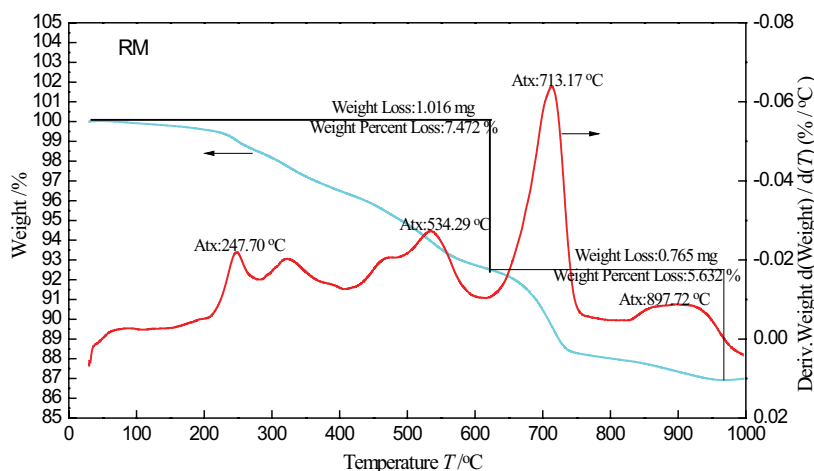


Fig. 3. Thermogravimetric analysis curves of RM.

Table 1
Composition of the PW from the phosphate ore flotation tailings reservoir

BOD/mg L ⁻¹	P/mg L ⁻¹	SO ₄ ²⁻ /mg L ⁻¹	F ⁻ /mg L ⁻¹	Cl ⁻ /mg L ⁻¹
8.4	156.7	154.4	3.3	9.85
Ca ²⁺ /mg L ⁻¹	Mg ²⁺ /mg L ⁻¹	AN/mg L ⁻¹	SS/mg L ⁻¹	pH
23.8	42.3	5.95	14.6	6.8

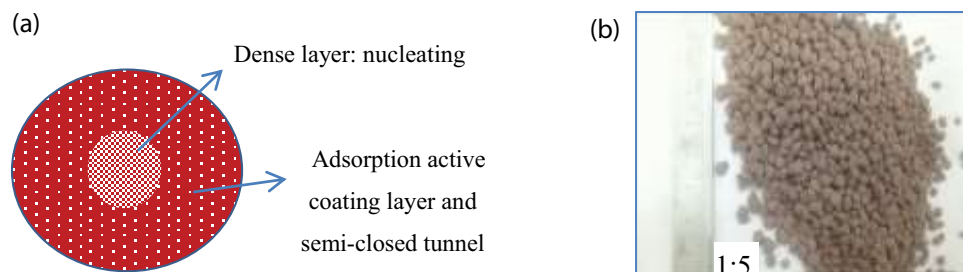


Fig. 4. (a) ARMFA model and (b) laboratory-prepared particulate adsorbent.

a two-layer structure, and the inner layer was a nucleating support body with a particle size of less than 1 mm. It was relatively dense, and its powdering rate was less than 1% at 24 h; the strength was greater than 2 KPa, and it had good surface wettability and stickiness. The external layer was the adsorption active coating layer, which had more adsorption active sites, a larger specific surface area, good wettability, certain strength, and good anti pulverization property. Blocked by the nucleation core, the pores were semi-via holes, which are more favorable to physical or chemical adsorption than through-holes. As the particle adsorbent had nucleating particle support, it was easy to prepare particles with high sphericity, good mechanical properties, and, thus, good adsorption stability. When preparing the particle adsorbent, the particle size, weight, specific surface area, strength, and powdering rate of each layer were designed first, and then, the nucleation support body, followed by the adsorption active coating layer, was prepared.

2.2.2. Preparation of bonding active liquid

The main roles of the binder active solution were to change the pH and zeta potential of the complex system; adjust the adsorption heat release rate of the adsorbent; change the apparent morphology of the adsorbent; adjust the specific surface area, pore-volume, and pore distribution; and adjust the particle strength and water immersion rate. For the test group, 105 ml of deionized water was added, followed by HPMC as the binder at mass fractions of 0.5%, 1%, 1.5%, 2.0%, and 2.5%. After magnetic stirring for 5 min, the effect of HPMC on the performance of the adsorbent particles was evaluated. Then, hydrochloric acid (2 mol L⁻¹) at mass fractions of 0.03%, 0.06%, 0.09%, 0.12%, and 0.15% was added, followed by magnetic stirring for 5 min. The effect of the various amounts of HCl on the performance of the adsorbent particles was studied. Subsequently, the pore modifier H₂O₂ at mass fractions of 0.2%, 0.4%, 0.6%, 0.8%, and 1.0%

was continuously added; the mixture was magnetically stirred for 5 min, and the effect of the various amounts of H_2O_2 was determined.

2.2.3. Preparation of nucleation particle support

RM and C_2S (mass ratio of 6:4) was placed in a high-speed powder dispersion mixer for mixing before being moved to a disc granulator for molding. During the molding process, the rotation speed of the disk was 90 rpm, and a certain amount of deionized water was added by a sprayer until the molding work was completed. After molding, the product was sieved by a sieve with a mesh size of 1 mm; then, the undersized proportion was placed in a constant temperature electric drying oven (at 40°C) and dried to a moisture content of <5%.

2.2.4. Preparation of particle adsorbent

RM, FA, MnO_2 , and other raw materials were placed into a high-speed powder disperser for mixing. The total mass of the test materials was about 300 g. Then, FA was added at mass fractions of 1.7%, 3.4%, 5.1%, 6.8%, and 8.5%, and the mass ratio of $MnO_2:H_2O_2$ was kept at 1:5. The nucleating particle support was added at a certain proportion, and then the disc granulator was started, the main ingredients were added, and the prepared adhesive active liquid was rotated. During the molding process, the additional speed and addition amount of the bonding active liquid was controlled until the adsorption active coating layer reached a certain thickness. Afterward, it continued to rotate for 10 min. The product was placed into a standard cement concrete curing box for 3 d with a constant temperature of 295 K–298 K and a humidity of 80%. After curing, the product was dried at 313 K.

2.3. Test methods

2.3.1. Adsorption test

Approximately 1,000 ml of phosphorus-containing wastewater was placed into a 1,500 ml beaker, and then 25 g of the ARMFA adsorbent was placed in the beaker after slight handshaking. Afterward, 5 ml of supernatant from the beaker was taken after 2, 4, 6, 8, and 10 h; each water sample was diluted to 15 ml with deionized water, and the P content was measured. The pH variation of the test solution was tracked in the beaker with a pH meter. Finally, the phosphorus removal rate η , adsorbent adsorption amount Q , and powdering rate η_m were calculated via formulas 1–3 as follows [23,24]:

$$\eta = \frac{C_0 - C_i}{C_0} \times 100\% \quad (1)$$

$$Q = \frac{V(C_0 - C_i)}{m} \times 100\% \quad (2)$$

$$\eta_m = \frac{m - m_i - m_s}{m} \times 100\% \quad (3)$$

where η is the phosphorus removal rate in the solution (%), C_0 is the phosphorus concentration in the solution before adsorption ($mg L^{-1}$), C_i is the phosphorus concentration in the solution after adsorption ($mg L^{-1}$), η_m is the powder pulverization rate (%), m_i is the dry weight of the adsorbent after adsorption (g), and m_s is the adsorption weight (g).

2.3.2. Product characterization methods

The content of P and other ions in the PW was determined by the yttrium internal standard method using an inductively coupled plasma emission spectrometer (ICP7400, Thermo Fisher Scientific, USA). The specific surface area, pore-volume, and pore size of the particulate adsorbent were tested using an N_2 adsorption-desorption physical adsorption instrument (ASAP2020, Micromeritics, USA), in which the specific surface area was calculated by the Brunauer-Emmer-Teller method, while the pore volume was calculated by the Barrett-Joyner-Halenda model from the isothermal adsorption branch. Specifically, the pore volume was calculated by the adsorption amount at the relative pressure $P/P_0 = 0.975$. The determination of particle strength was conducted using an APT-3 particle strength tester. The chemical composition of the samples was determined using an X-ray fluorescence (XRF) spectrometer (Axios mAX, 4 kW, PANalytical B.V., Netherlands). The phase and crystal structure of the sample was characterized via an X-ray diffractometer (POWDER PRO, PANalytical, Netherlands) using a Cu target K_α source ($\lambda = 0.154$ nm), a tube voltage of 40 kV, and a tube current of 40 mA. The test used a step scan with a step size of 0.05, a scan speed of $0.5^\circ/s$, and a scan range of 10° – 70° . The surface structures of the RM original sample and particulate adsorbent were observed by an S-3400 scanning electron microscopy (SEM) manufactured by Japan Tianli Co. Ltd., and the test operating voltage was 20 kV. The functional groups contained in the samples before and after adsorption were characterized by a VERTEX 70v Fourier infrared spectroscopy (FT-IR) analyzer from Bruker, Germany. A solid infrared method was applied as follows: a small amount of sample (about 0.6 mg) and 200 mg of potassium bromide were uniformly ground in an agate mortar and compressed and subjected to an FT-IR test with a wavenumber range of 4,000–400 cm^{-1} . The surface zeta potential of the sample and adsorbent was measured using a nanoparticle size/zeta potential analyzer (DelsaNano C, Beckman Coulter, USA). The heat value of the adsorption process of the adsorbent was measured using a microcalorimeter (C80, Setaram, French). Then, X-ray photoelectron spectroscopy (XPS) (AXIS ULTRADLD, Kratos, Shimadzu Group, Monochromated Al Target, 150 W) was used to scan the particle samples before and after adsorption to analyze the composition changes of the surface materials of the adsorbents. The relative content and bonding mode of phosphorus (P 2p) in the particle sample after adsorption of phosphate were analyzed to reveal the mechanism of action of the phosphorus on the surface of the adsorbent.

2.3.3. Adsorption kinetic analysis

The adsorption rate of the total P was evaluated by primary and secondary kinetic models. The expressions of the

pseudo-first-order dynamic equation and pseudo-second-order dynamic equation of the Lagergren equation were as follows [25].

$$\log(Q_e - Q_t) = \log Q_e - \frac{k_1}{2.303} t \quad (4)$$

$$\frac{t}{Q_t} = \frac{1}{k_2 Q_e^2} + \frac{1}{Q_e} \quad (5)$$

where Q_e is the adsorption amount of P at equilibrium (mg g^{-1}), Q_t is the amount of adsorption of P at the time of t (min) (mg g^{-1}), k_1 is the rate constant of first-order kinetic adsorption, and k_2 is the second-order kinetic adsorption constant; k_2 could be calculated from the slope and intercept of curve t/Q_t , and the adsorption rate constant could be determined from the slope in a linear graph of $\log(Q_e - Q_t)$ vs. t .

2.3.4. Adsorption equilibrium isotherm

The phosphorus-containing wastewater was filtered through a 45 μm filter membrane and diluted to solutions with a phosphorus content of 20, 25, 30, 40, 50, 65, 90, 120, and 150 mg L^{-1} via stepwise dilution. Then, 0.1 mol L^{-1} NaOH were used to adjust the pH to around 8. To ensure that the adsorption reached equilibrium, the reaction time was set at 10 h, and the temperature was 298 K. The adsorption isotherm of the ARMFA was determined separately and, thus, fitted respectively. The adsorption capacity of the adsorbent was determined by the Freundlich, Langmuir, and Temkin isothermal models. The mathematical expressions of the kinetic models are as follows [26,27]:

$$Q_e = K_f C_e^{1/n} \quad (6)$$

$$\frac{C_e}{Q_e} = \frac{1}{bQ_m} + \frac{C_e}{Q_m} \quad (7)$$

$$Q_e = \frac{RT}{b_T} \ln K_T + \frac{RT}{b_T} \ln C_e \quad (8)$$

where Q_e (mg g^{-1}) is the adsorption amount of P by unit mass of adsorbent, C_e (mg g^{-1}) is the concentration of P at equilibrium, K_f is the Freundlich constant related to the adsorption capacity, n is the Freundlich constant indicating the adsorption intensity, Q_m (mg g^{-1}) is the maximum adsorption capacity, b (L mg^{-1}) is the Langmuir constant, b_T (L mg^{-1}) is the Temkin constant, R is the gas constant, T (K) is the adsorption temperature, and K_T is the Temkin constant related to adsorption capacity.

3. Results and discussion

3.1. ARMFA preparation and performance testing

3.1.1. Adsorption effect of unmodified RM

Unmodified RM was granulated and formed according to the method described in Section 2.3, and the phosphate in the

backwater of the tailings dam was adsorbed. After adsorption, the adsorption capacity, removal rate, particle compressive strength, and soaking pulverization rate for 24 h were tested and comprehensively evaluated. When the adsorption temperature was 298 K–303 K and the adsorption time was 14 h, the adsorption capacity of total phosphorus was 20.53 mg g^{-1} , the removal rate was 40.16%, the compressive strength was 0.36 KPa, and the soaking rate was 87.40%, indicating that unmodified RM has a certain adsorption capacity for total phosphorus. It was found that the inactivated RM contained a certain combination of water and organic matter that was smaller than the surface, with poor cementing performance, and fewer active adsorption sites, leading to a poor adsorption effect. However, it could be modified by activation and enhanced by mechanical properties.

3.1.2. Effect of FA on the adsorbent performance

As shown in Fig. 5, when the adsorption temperature was 298 K and the adsorption time was 14 h, the adsorption effect of RM on P was not satisfactory, and the removal rate was only 62.62%. In addition, from Fig. 6, the particle adhesion was unsatisfactory, the strength was only 0.36 KPa, the particles placed in the PW were disintegrated and eroded, and the pulverization rate was as high as 87.4% in 24 h. After the addition of FA, the removal rate of total P gradually increased. However, the FA reduced the viscosity of the adsorbent and lowered the strength. For example, when 8.3% of FA was added, the removal rate of P reached 76.6%, while the powdering rate reached 94.30%. The addition of FA increased adsorption active substances such as Al_2O_3 and Fe_2O_3 , thus increasing the specific surface and active sites of the adsorbent. However, the adhesion of the FA was poor, resulting in a decrease in the true density of the particles and a loose structure. This lowered the particle strength and increased the powdering rate.

3.1.3. Effect of HPMC on the adsorbent performance

To increase the strength and reduce the immersion pulverization rate of the adsorbent, HPMC was added as a

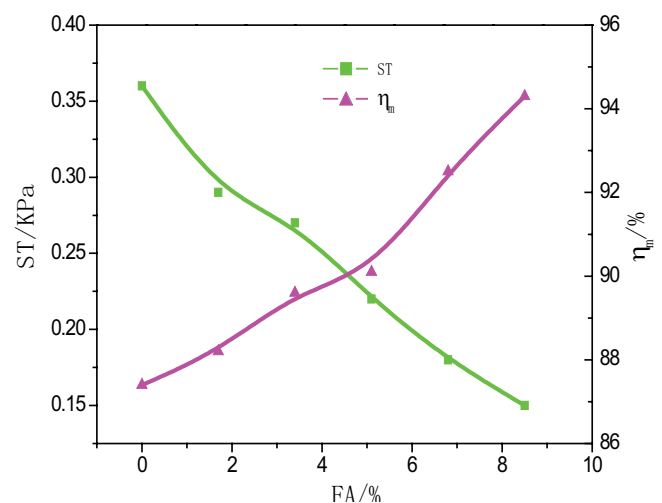


Fig. 5. Effect of FA on the adsorption capacity and removal rate of adsorbent.

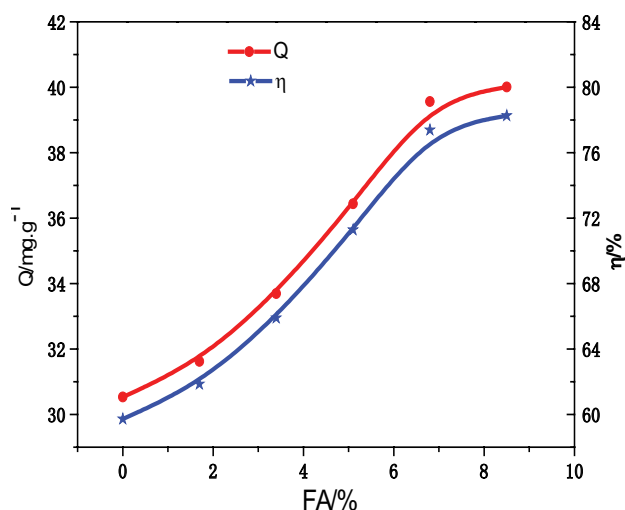


Fig. 6. Effect of FA on the compressive strength and the immersion pulverization rate of adsorbent.

binder on the basis of adding FA. As shown in Figs. 7 and 8, under the same conditions, the adsorption capacity of the adsorbent to P decreased with the addition of HPMC. When the dosage of HPMC increased from 0.05% to 0.25%, the removal rate of P by the adsorbent decreased from 79.69% to 68.95%, but the strength increased from 0.58 to 0.81 KPa. Moreover, the pulverization rate of the particles decreased to 3.5% when the dosage of HPMC was 0.25%. The water and HPMC formed a sol during the granulation of the adsorbent, which increased the consistency and viscosity of the binder. At the same time, HPMC and solid particles formed a network-like structure after hydration, increasing the contact angle of the surface of the particles and partially filling it and reducing the adsorption capacity. This property of HPMC increased the strength of the particulate adsorbent and the rate of soaking loss and also improved the adsorption stability of the adsorbent.

3.1.4. Effect of C_2S on the adsorbent performance

As shown in Figs. 9 and 10, the compressive strength and immersion pulverization rate of the adsorbent with HPMC added still failed to meet the requirements. Therefore, C_2S was added as a strength enhancer to increase the compressive strength and reduce the immersion pulverization rate of the adsorbent via synergistic action with HPMC. It is a high-performance cement with a low environmental load that contains over 50% dicalcium silicate. It is characterized by a low hydration heat, high strength, and fast hydration time. When the amount of C_2S increased from 1% to 5%, the compressive strength of the adsorbent increased from 0.93 to 1.42 KPa and the immersion pulverization rate reduced from 3% to 1.2%. However, at the same time, the removal rate of P decreased from 70.35% to 60.21%. Overall, after adding C_2S during the granulation process, the granules were quickly hydrated and the processing time was shortened. However, the addition of C_2S increased the compactness of the particles, and some of the pores were blocked, resulting in a decrease in the adsorption capacity.

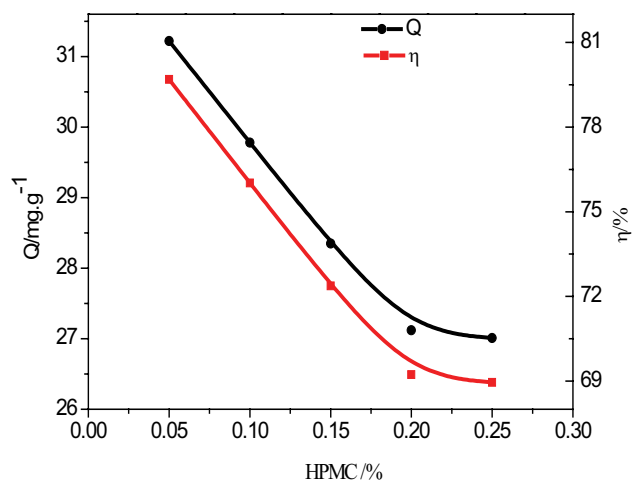


Fig. 7. Effect of HPMC on the adsorption capacity and removal rate of adsorbent.

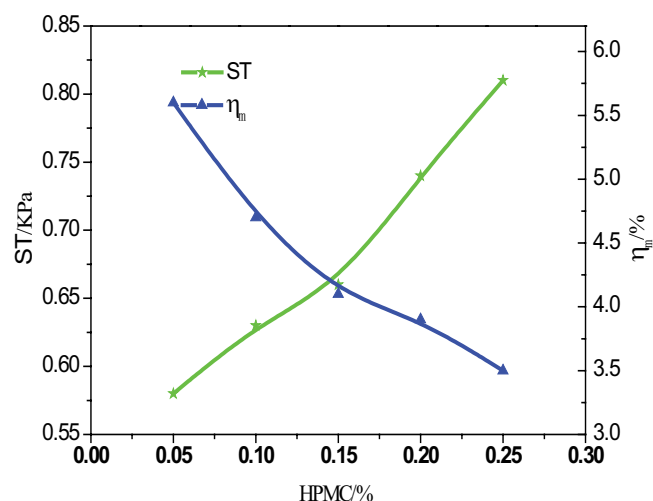


Fig. 8. Effect of HPMC on the compressive strength and the immersion pulverization rate of adsorbent.

3.1.5. Effect of $H_2O_2 + MnO_2$ on the adsorbent performance

While the particle strength increased but the pulverization rate decreased, the adsorption effect weakened again. It can be seen from Figs. 11 and 12 that the addition of $H_2O_2 + MnO_2$ as a pore-forming agent increased the adsorption capacity of the adsorbent from 76.91% to 93.71%. MnO_2 is a catalyst for the decomposition of H_2O_2 . Under alkaline conditions, $H_2O_2 + MnO_2$ can generate a large number of microbubbles, dredge the channels of adsorption sites, and expose larger adsorption surfaces. Both H_2O_2 and MnO_2 have a good oxidation performance that lowers the metal valence state and, thus, increases the adsorption activity point during the adsorption process. However, the strength of the particle adsorbent decreased sharply due to the generation of microbubbles, leading to a large mass loss during immersion. This had a certain adverse effect on the repeated regeneration of the adsorbent.

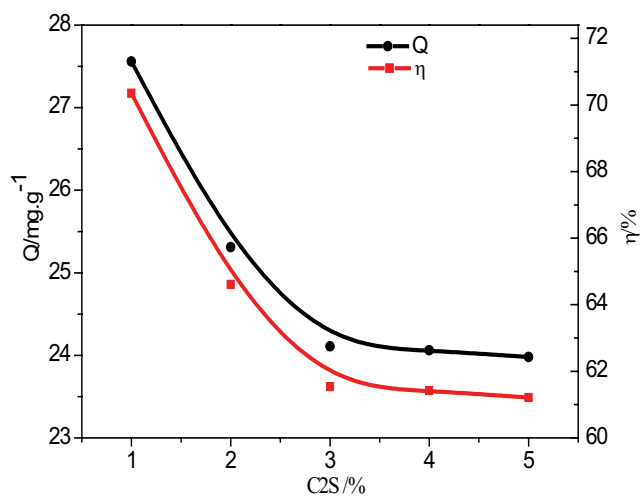


Fig. 9. Effect of C₂S on the adsorption capacity and removal rate of adsorbent.

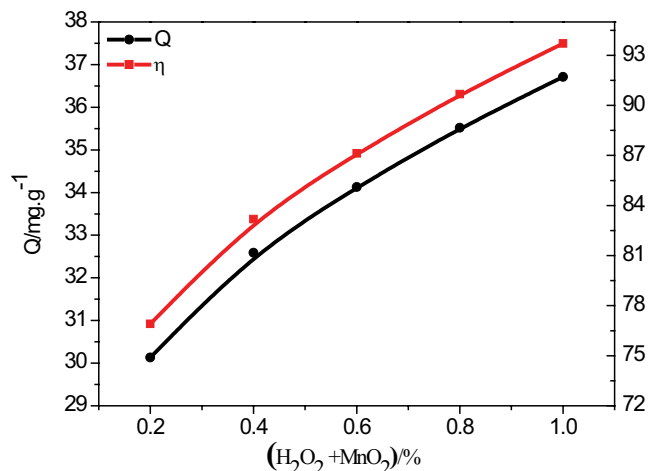


Fig. 11. Effect of H₂O₂ + MnO₂ on the adsorption capacity and removal rate of adsorbent.

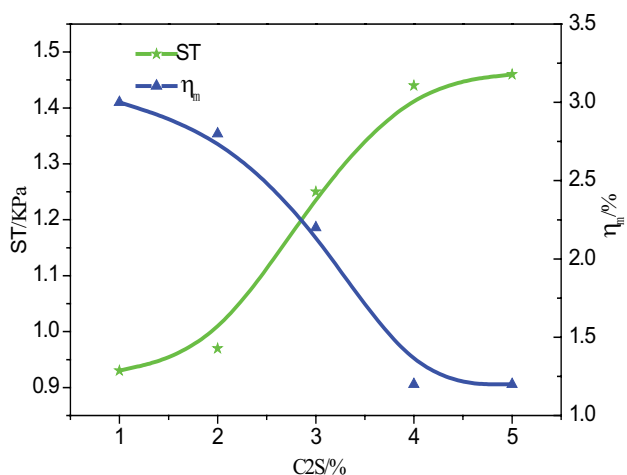


Fig. 10. Effect of C₂S on the compressive strength and the immersion pulverization rate of adsorbent.

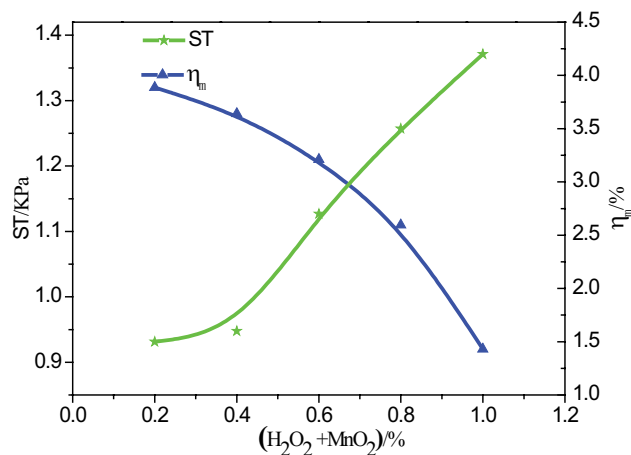


Fig. 12. Effect of H₂O₂ + MnO₂ on the compressive strength and the immersion pulverization rate of adsorbent.

3.1.6. Effect of HCl on the adsorbent performance

As shown in Figs. 13 and 14, the porosity was improved by HCl activation and the addition of the H₂O₂ and MnO₂ foaming agent. The removal rate of phosphorus reached 98.12%, the strength was 1.03 KPa, and the 24 h immersion pulverization rate was <5%. HCl is a strong monobasic acid that releases a large amount of H⁺ in binders. It activates minerals, which changes the pore structure of adsorbents, removes impurities in the pores, and facilitates the entry and adsorption of pollutant molecules. When the amount of HCl increased, the adsorption capacity of the adsorbent first increased and then decreased; the adsorption performance was best when the added amount was 0.5%. After that, as the HCl dosage increased, the adsorption capacity decreased. This occurred because, during the granulation process, HCl dissolved K⁺, Ca²⁺, Na⁺, Fe²⁺, and Al³⁺ in the adsorbent, eliminating the original interlayer bond force and causing cracking of the crystal lattice layer [20]. When the amount of HCl

increased, the OH⁻ and H⁺ in the system were neutralized; thus, through pores were partially formed, which reduced the adsorption capacity. At this time, the strength of the adsorbent decreased, and the immersion pulverization rate increased.

3.2. Performance optimization and testing

To achieve the best adsorption performance, we kept the amount of RM, FA, and water unchanged and performed a four-factor to three-level orthogonal test with HPMC, C₂S, H₂O₂ + MnO₂, and HCl as variables. The test results are shown in Table 2. The order of the range of the difference was as follows: (1) influencing factors of the adsorption amount were B > D > C > A, and, thus, the optimal design was B3D3A2C2; (2) influencing factors of strength were A > C > D > B, and, thus, the optimal design was B2A2C3D2. Considering the cost and effect, B3A2C2D3 was chosen as the optimal design. Considering the effects of the adsorption amount, removal rate, particle strength, and 24 h soaking powdering rate, we

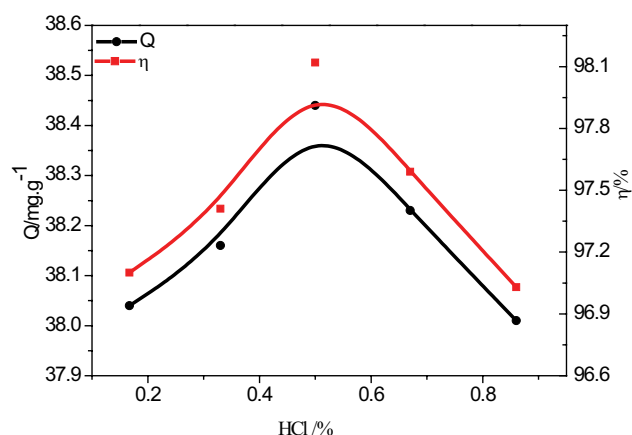


Fig. 13. Effect of HCl on the adsorption capacity and removal rate of adsorbent.

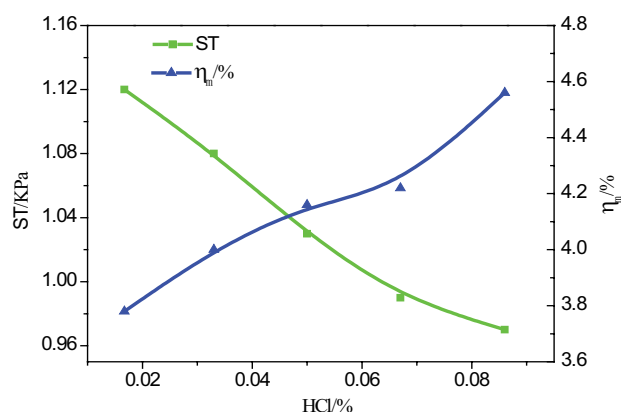


Fig. 14. Effect of HCl on the compressive strength and the immersion pulverization rate of adsorbent.

Table 2
Four-factor to three-level orthogonal test results

No.	A	B	C	D	<i>j</i> , adsorption capacity/ (mg g ⁻¹)	<i>i</i> , intensity/ KPa
	HPMC/%	(H ₂ O ₂ + MnO ₂)/%	C ₂ S/%	HCl/%		
1	0.1	0.27	3	0.09	35.82	0.89
2	0.1	0.80	4	0.17	37.65	0.97
3	0.1	1.00	5	0.26	38.04	0.96
4	0.15	0.27	4	0.26	36.72	1.27
5	0.15	0.80	5	0.09	37.05	1.31
6	0.15	1.00	3	0.17	38.46	1.23
7	0.2	0.27	5	0.17	36.39	1.11
8	0.2	0.80	3	0.26	38.43	1.13
9	0.2	1.00	4	0.09	37.41	1.12

found that the best ratio (mass ratio) of the ARMFA particle adsorbent was RM:FA:water = 19:1:7, and 0.15% HPMC, 0.17% HCl, 4% C₂S, 1% H₂O₂, and 0.2% MnO₂. The pH, specific surface area, and pore volume of the ARMFA particle adsorbent prepared under the above conditions were 9.25, 40.54 m² g⁻¹, and 2.10 cm³ g⁻¹, respectively. For the PW with an initial total P concentration of 156.7 mg L⁻¹, when the amount of ARMFA was 25 g L⁻¹ and the adsorption time was 14 h, the adsorption amount was 38.46 mg g⁻¹, the removal rate of P was 98.17%, the strength was 1.31 KPa, and the 24 h soaking powdering rate was 3.72%.

Table 3 compares the results of similar studies. Many studies have shown that its adsorbents are phosphorous preparations. In this study, phosphorus separation tailwater from an actual phosphate ore dressing plant was used. The ARMFA adsorbed total phosphorus up to 38.46 mg g⁻¹, indicating a good adsorption effect.

3.3. Analysis of the adsorption mechanism

3.3.1. pH variation of the adsorption system

The pH of the RM and particulate adsorbent ARMFA were 10.35 and 9.35, respectively. As the adsorption time increased, the pH of the ARMFA decreased to about 8.45

(Fig. 15a). The original pH of the PW was 6.80, and this figure increased to about 8.50 after 10 h of adsorption (Fig. 15b). Therefore, as time increased, the pH of the entire adsorption system tended to be between 8.45 and 8.52. This was because of a large number of alkaline substances in the RM (sodium hydroxide, sodium bicarbonate, sodium carbonate, sodium aluminate, calcite, sodalite, hydrated garnet, etc.) were encapsulated by HPMC and C₂S after being made into a particulate adsorbent, exhibiting a relatively lower initial pH. However, when the adsorbent was immersed in the PW, the alkaline substances were hydrolyzed to produce OH⁻ ions, resulting in an increase in pH. The OH⁻ released by the adsorbent combined with the H⁺ in the PW and, finally, the pH of the system stabilized.

3.3.2. Chemical composition during the adsorption process

As shown in Table 4, the content of the components in the ARMFA related to adsorption performance (such as Fe₂O₃ and Al₂O₃) obviously increased. After adsorption, the P₂O₅ content in the ARMFA increased, indicating that P was successfully adsorbed. However, the content of CaO, Al₂O₃, Fe₂O₃, and K₂O in the ARMFA decreased, indicating that the alkaline matter decreased after adsorption and formed (Al₂O₃)₁₀(MgO)₁₀(Na₂O)₁₀(P₂O₅)₇₀ CaHPO₄ Na₂HPO₄, and other

Table 3
Comparison of research results

Adsorbent	Adsorbate	Adsorption quantity (mg g ⁻¹)	References
Fe ₃ O ₄	KH ₂ PO ₄	20	[28]
Chitosan/Ca-organically modified montmorillonite	H ₃ PO ₄	76.15	[29]
Oxygen furnace slag	KH ₂ PO ₄	21–30	[30]
PVA-CSH	KH ₂ PO ₄	31.06	[31]
Fe-loaded ceramics	NaH ₂ PO ₄	45.88	[32]
Brine modified red mud	KH ₂ PO ₄	12.89	[33]
New adsorption material for red mud particles	KH ₂ PO ₄	20.60	[34]
ARMFA	Phosphate ore flotation tailings reservoir total P	38.46	This paper

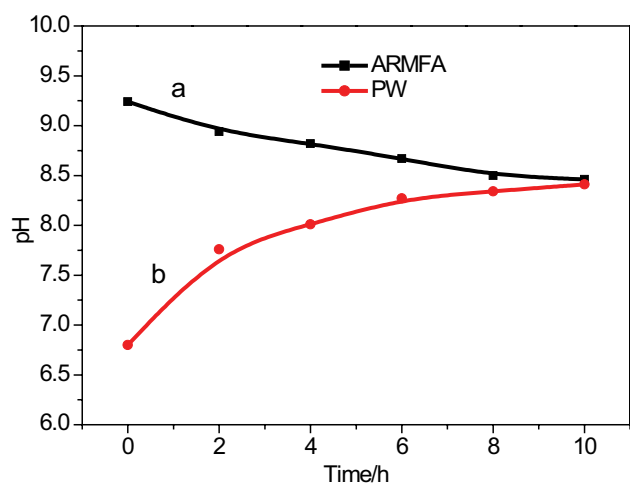


Fig. 15. pH of ARMFA and PW with a variation of adsorption time.

substances. The pH was also observed to have a downward trend, consistent with the pH test results in Fig. 15.

3.3.3. Surface topography analysis

As shown in Fig. 16, there were small pores on the surface of the RM, and a powdery substance filled around the pores was observed. The specific surface area was relatively small (Fig. 16a). Meanwhile, for the ARMFA, the surface was rough, the pores were evenly distributed, and the specific surface area was relatively large (Fig. 16c). It can be seen from Figs. 16b and d that before adsorption, the ARMFA had an irregular surface with a loose structure and large inter-particle gaps, comprising the gap between the aggregate, the agglomerate, and the aggregate. The surface material mainly consisted of voids between aggregates, agglomerates, and aggregates. During the comprehensive modification of the ARMFA particle adsorbent, the surface was eroded, causing the ARMFA to display a rougher surface and richer pores. In addition, the loose porosity of FA made the surface pores of the particles more developed, improving the adsorption capacity of the ARMFA. After adsorption, there were fewer

pores on the surface of the ARMFA, and the bulk and flocculent substances increased. This happened because the ARMFA was soaked and eroded by the PW and hydrolysis occurred, causing the material around the pore to collapse, deposit, and form a lump. In addition, Ca²⁺/Na⁺/Al³⁺/Mg²⁺ adsorbed P and phosphate and adhered to the surface of the pores, causing the surface of the adsorbent to become massive and flocculated.

3.3.4. Zeta potential and infrared spectrum analysis

To further reveal the adsorption mechanism, the zeta potentials of the RM and ARMFA at different pH values were determined. The results are shown in Fig. 17. It was found that the zero-point pH for ARMFA was 3.2; when the pH was <3.2, the ARMFA surface was positively charged and repelled with the total P. As shown in Fig. 17, at pH 4–9, the zeta potential of the ARMFA had a smaller absolute value than the zeta potential of the RM, indicating that the adsorption capacity of the ARMFA on anions was stronger than that of the RM at pH 4–9 after modification. The FT-IR spectrum of the ARMFA before and after adsorption is shown in Fig. 18. The peak at the frequency of 1,114 cm⁻¹ was a Si–O–Si group, at 1,456 cm⁻¹ were a carboxylate COO⁻ group and CO₃²⁻ group, and at 995 cm⁻¹ was the peak spectrum of the POP group. The peak at the frequency of 3,600–3,000 cm⁻¹ was crystal water; most of the substances did not change before or after adsorption. The strong peak at 1,156 cm⁻¹ after adsorption was the PO₄³⁻ group, indicating that the adsorbent had loaded P in PW.

3.3.5. XPS analysis

According to the results of the XRF, X-ray energy spectrum analysis (EDS), and FT-IR, the ARMFA successfully adsorbed P from the PW. To determine the composition of the adsorbed material and the form of the adsorbed P, the sample was subjected to an XPS analysis. The XPS spectrum of the sample after adsorption is shown in Fig. 19. As can be seen from the figure, the surface of the sample mainly included Fe 2p, Al 2p, Ca 2p, Ti 2p, Si 2p,

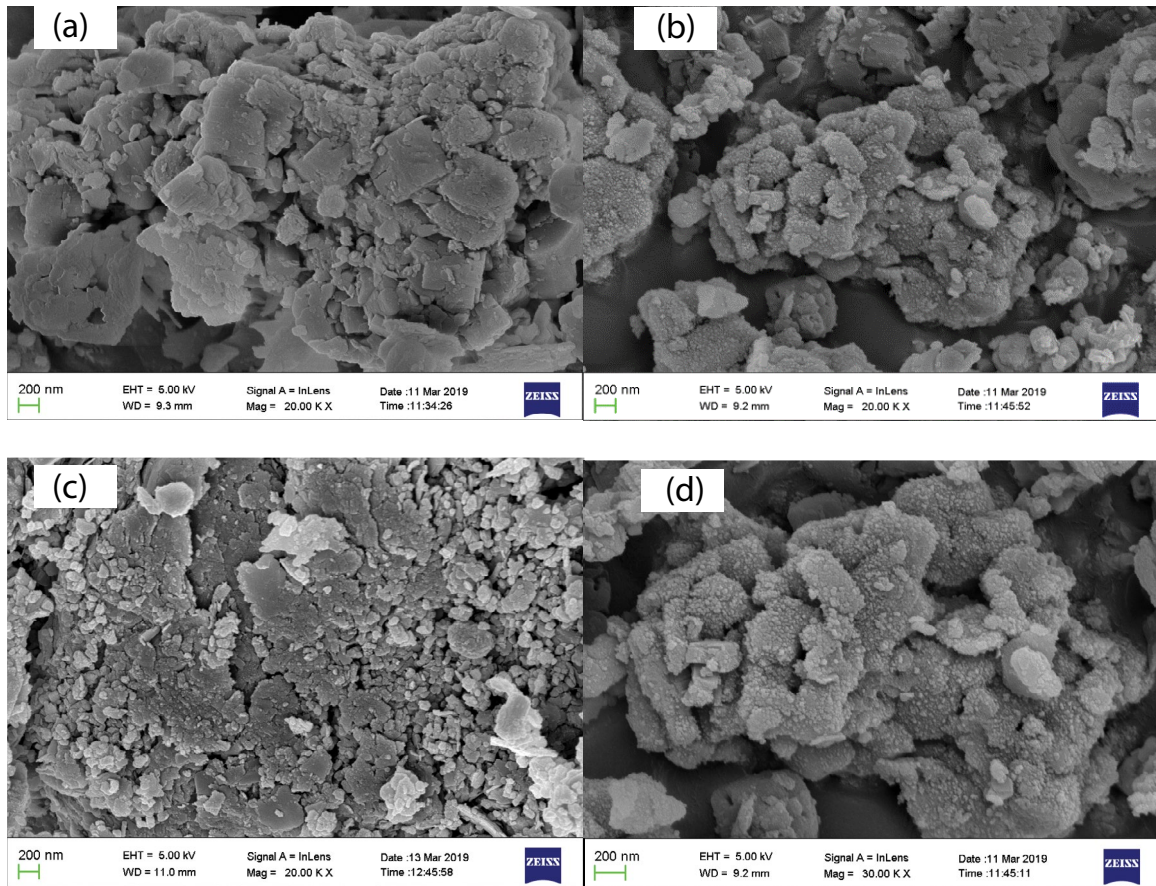


Fig. 16. Surface morphology of ARMFA and RM under SEM; (a) particle surface of RM, (b) RM after adsorption, (c) particle surface of ARMFA, and (d) ARMFA after adsorption.

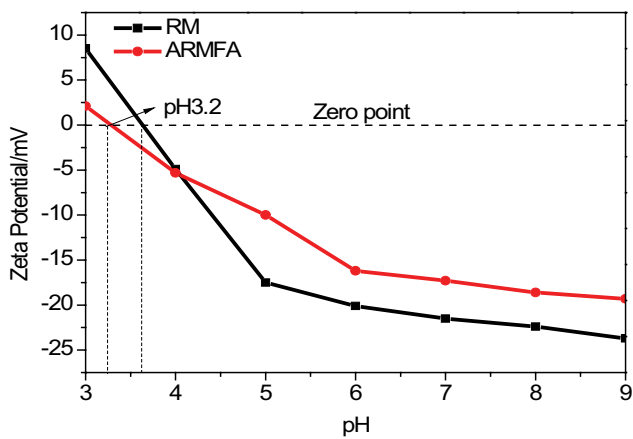


Fig. 17. Relationship between zeta potential and pH of adsorbent.

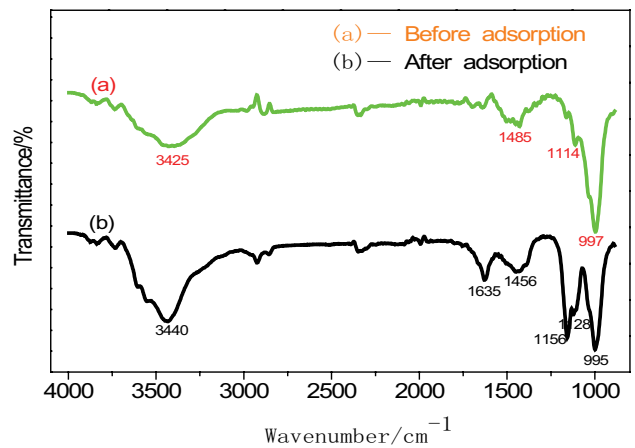


Fig. 18. Infrared spectrum before and after adsorption by ARMFA.

K 2p, Na 1s, Mg 1s, etc. In particular, there was no P 2p spectrum on the surface of the ARMFA sample before adsorption (Fig. 19a), but after adsorption, it had a P 2p spectrum at 133.7 eV (Fig. 19b), indicating that the phosphorus had been successfully adsorbed on the surface of the ARMFA, consistent with the XRF results.

An XPS analysis of the ARMFA particle adsorbent after adsorption was performed. The results are shown in Fig. 20,

and the peaking results are shown in Table 4. Before adsorption (Fig. 20a), the characteristic spectrum of P 2p on the surface of ARMFA was unclear. Combined with the XRD data, the binding energy had a small amount of $\text{Ca}_{10}(\text{PO}_4)_6(\text{OH})_2$ at 133.2 eV; however, after adsorption (Fig. 20b), the binding energy of P 2p existed in three forms, as shown in Table 5. The binding energy had one obvious characteristic peak at 133.2 eV, and its existence form was $(\text{PO}_4)_2 \cdot 3\text{H}_2\text{O}$, Na_2HPO_4 ,

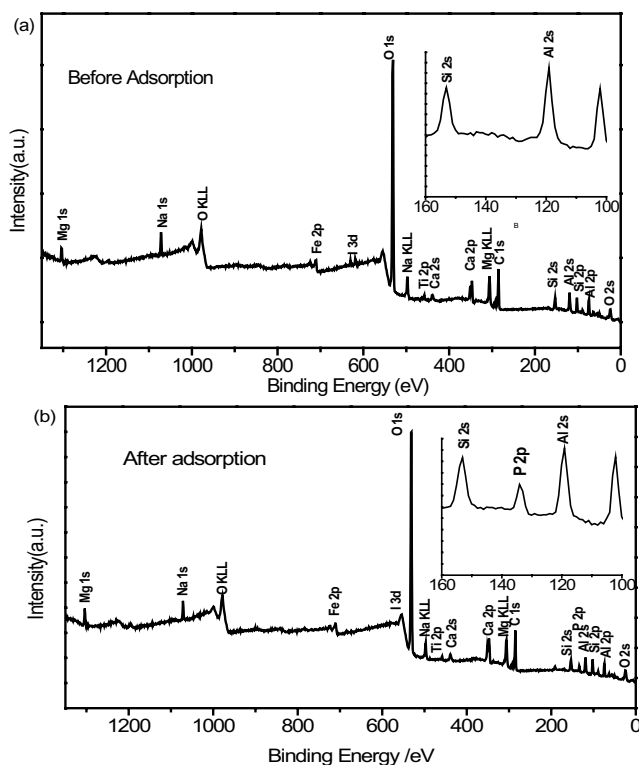


Fig. 19. (a) XPS photoelectron spectroscopy before and (b) after adsorption.

Table 4
XRF analysis before and after adsorption

Oxidizing substance	RM/Wt. %	ARMFA/Wt. %	ARMFA after adsorption/Wt. %
Fe ₂ O ₃	21.94	22.32	21.67
Al ₂ O ₃	21.04	20.05	20.51
SiO ₂	19.50	19.79	18.54
CaO	17.95	18.62	19.04
Na ₂ O	8.96	8.66	6.40
TiO ₂	5.90	5.55	5.11
MgO	1.58	1.50	2.19
K ₂ O	1.34	1.33	1.10
SO ₂	0.392	0.372	0.289
P ₂ O ₅	0.377	0.360	3.96
ZrO ₂	0.314	0.315	0.298
SrO	0.182	0.169	0.159

and the corresponding ratio was 38.51%. The binding energy had another obvious characteristic peak at 134.2 eV, and its existence form was (Al₂O₃)₁₀(MgO)₁₀(Na₂O)₁₀(P₂O₅)₇₀, and the corresponding ratio was 48.34%. Finally, the binding energy had its last weak characteristic peak at 133.2 mV; its existence form is CaHPO₄, and the corresponding ratio was 13.15%. It was indicated that in the adsorption system when the pH was 8–9, P mainly existed in the form of HPO₄²⁻ and PO₄³⁻, which is consistent with the existing state of phosphate in an aqueous solution as reported in the literature. These ions

and positively charged Ca²⁺/Na⁺/Al³⁺/Mg²⁺ formed strong chemical bonds by precipitation, surface deposition, and ion exchange coordination and were distributed on the inner surface of the ARMFA tunnel.

3.3.6. Adsorption kinetic analysis and thermodynamic analysis

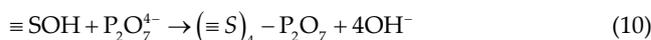
It can be seen from the comparison of the R² value in Table 6 that the results of data fitting using the pseudo-second-order dynamic model were better than those of the pseudo-first-order dynamic model; thus, the pseudo-second-order dynamic model could better describe the adsorption process for phosphorus by the ARMFA (shown in Fig. 21). Upon comparing the R² values in Table 7, it is obvious that the adsorption process of P by the ARMFA was more consistent with the Langmuir model, indicating that the main adsorption form of the first two adsorbents in the adsorption process was single-layer adsorption (shown in Fig. 22).

The results of the adsorption microcoria test of the RM and ARMFA are shown in Fig. 23. The RM and ARMFA adsorptions were both exothermic reactions, and the ARMFA micro heat value was -5.022 J g⁻¹ and greater than that of RM, indicating that the adsorption effect of the adsorbent after comprehensive modification was better than that before modification.

3.3.7. Adsorption process model

The adsorption system entailed complex dynamic adsorption processes between the RM particle adsorbent and phosphate ore wastewater containing phosphorus, including diffusion and penetration, surface hydroxylation, surface dissolution, adsorption, and flocculation.

When the ARMFA was placed into the PW, the adsorbent surface was in contact with the PW because the interaction between solid surface molecules and liquid is greater than that between liquid molecules. Liquid molecules gathered to the solid-liquid interface. The PW moistened the surface of the ARMFA and diffused and penetrated the internal pores of the ARMFA; the phosphorous liquid was brought into the pores. Due to the air hole contained inside the adsorbent, the PW diffusion penetrated to the back of the pore gas channel and produced inflation. The ARMFA bonding agent on the surface of the C–O bond ruptured, breaking the barrier of the potential energy surface. The surface pore richer, diffusion and permeation speed dissolved Ca²⁺, Fe²⁺, Al³⁺, and PO₄³⁻. Then, HPO₃²⁻ generated capacitive precipitation, that is, the main reaction shown in chemical formulas 9 and 10, where ≡S represents the adsorption site on the surface of RM.



The ARMFA contained a large amount of Fe³⁺ and Al³⁺ and had a high positive charge, which could effectively reduce the zeta potential of suspended particles in water, the thickness of the double electric layer, and the repulsive

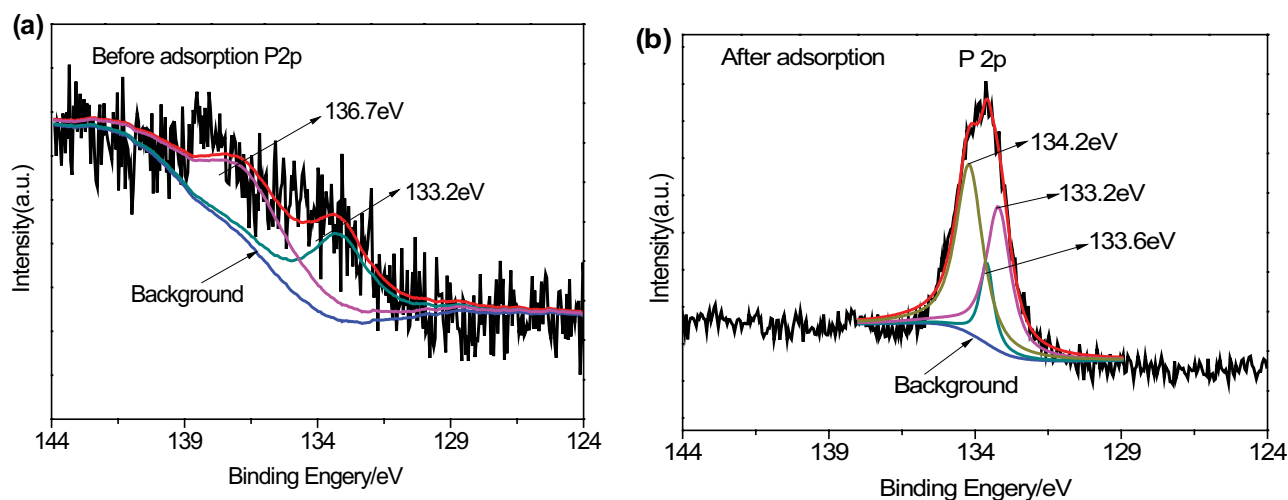


Fig. 20. (a) XPS photoelectron spectroscopy of P 2p before and (b) after adsorption.

Table 5
XPS of P 2p peak results

Name	BE/eV	Full width at half maxima (FWHM)	Area/CPS.eV	Combined state	Ratio/%
P 2p	133.2	1.02	852.89	$(\text{PO}_4)_2 \cdot 3\text{H}_2\text{O}/\text{Na}_2\text{HPO}_4$	38.51
P 2p	133.6	0.60	291.20	CaHPO_4	13.15
P 2p	134.2	1.02	1070.49	$(\text{Al}_2\text{O}_3)_{10}(\text{MgO})_{10}(\text{Na}_2\text{O})_{10}(\text{P}_2\text{O}_5)_{70}$	48.34

Table 6
Pseudo-first- and pseudo-second-order kinetic parameters of P adsorption by ARMFA

Kinetic model	Parameter 1	Parameter 2	R^2	T
Pseudo-first-order dynamic model	$k_1 = 0.2 \text{ (h}^{-1}\text{)}$	$q_e = 44.67 \text{ (mg g}^{-1}\text{)}$	0.9684	273 K
Pseudo-second-order dynamic model	$k_2 = 0.0402 \text{ (g mg}^{-1} \text{h}^{-1}\text{)}$	$q_e = 45.21 \text{ (mg g}^{-1}\text{)}$	0.9741	273 K

Table 7
Freundlich, Langmuir, and Temkin adsorption parameters of ARMFA

Thermodynamic model	Parameter 1	Parameter 2	R^2	T
Langmuir	$K_L = 0.156 \text{ (L mg}^{-1}\text{)}$	$q_{\text{max}} = 106.89 \text{ (mg g}^{-1}\text{)}$	0.9993	273 K
Freundlich	$K_F = 1.5796 \text{ (mg}^{(1-n)} \text{L}^n \text{g}^{-1}\text{)}$	$1/n = 0.6889$	0.9897	273 K
Temkin	$K_T = 0.6845 \text{ (L mg}^{-1}\text{)}$	$b_T = 0.02356$	0.9927	273 K

force and stability between phosphate particles. The particles could aggregate into flocculation and form a loose fibrous structure, thus generating flocculation precipitation.

3.3.8. Safety analysis of adsorbents for water treatment

To explore the safety of the use of solid adsorbent particles, a toxicity analysis was performed according to the Chinese National Standard HJ 557-2010 solid waste leaching toxicity method horizontal oscillation method. The measurement results are shown in Table 8. Compared with the heavy metal leaching results of the RM, the leaching concentrations of Pb, Cr, and Zn of the RMFA and ARMFA were significantly

reduced, indicating that C_2S had a certain curing ability for the abovementioned pollutants in the raw materials during the preparation of the adsorbent. At the same time, the heavy metal leaching rate of the RMFA and ARMFA met the Chinese National Standard GB5085.3-2007 “dangerous waste identification standard leaching toxicity identification” for the limits of Pb, Cd, Cr, Hg, and Zn. The safety as a water treatment material basically met the requirements as well.

4. Conclusions

In this study, the adsorption and mechanical properties of RM particles were improved via nonthermal activation.

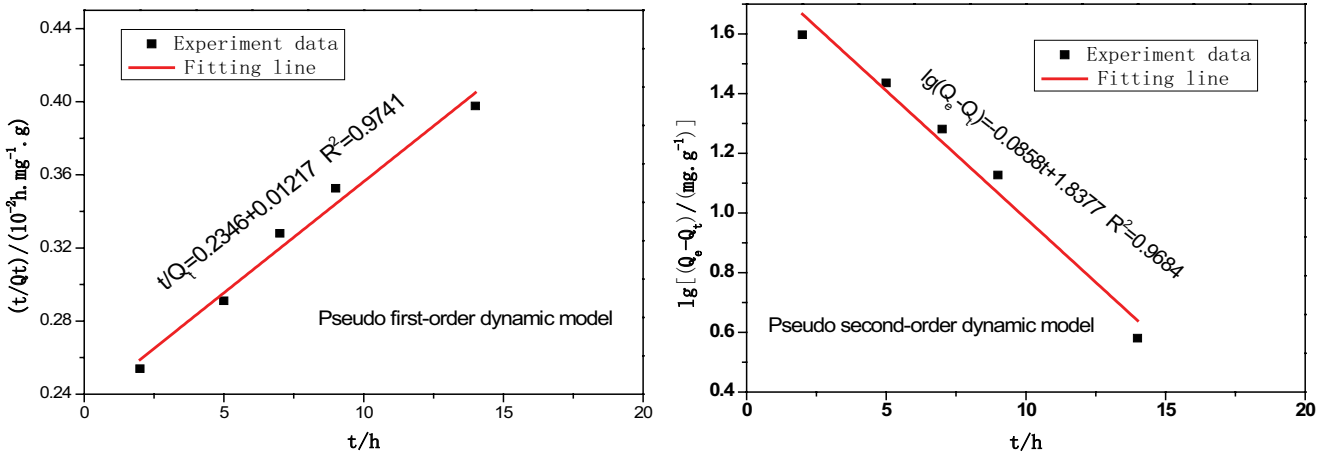


Fig. 21. Adsorption kinetic models.

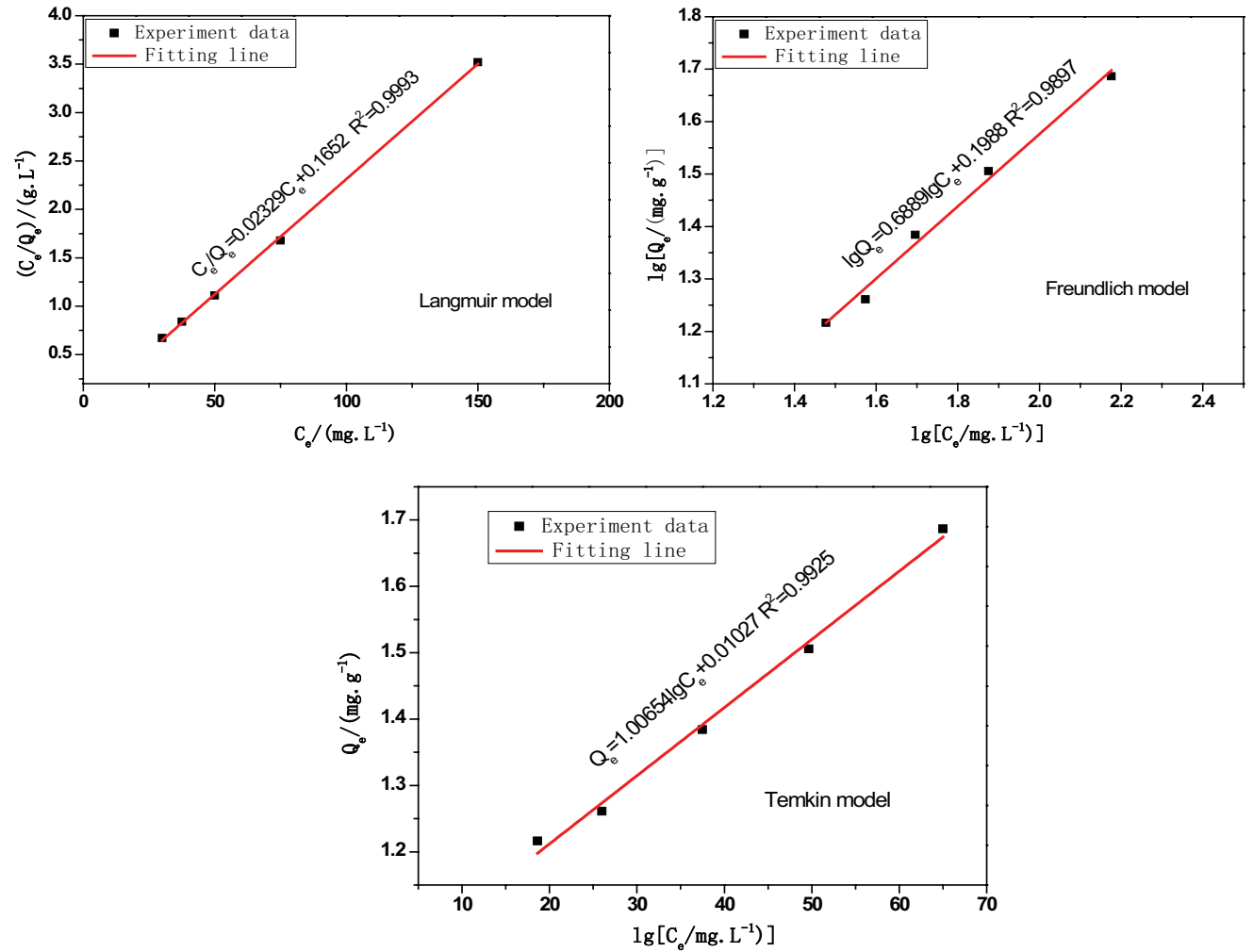


Fig. 22. Adsorption thermodynamic models.

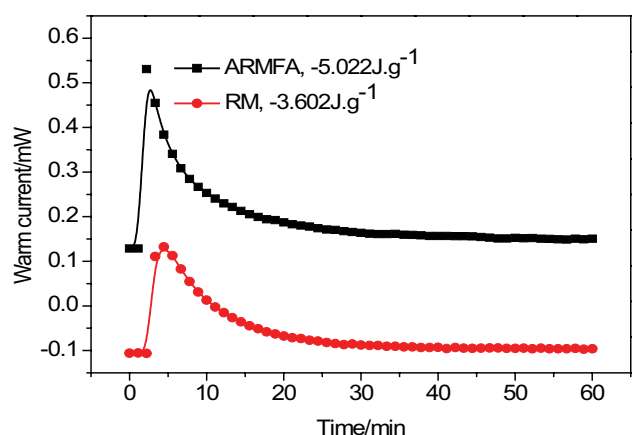


Fig. 23. Results of adsorption microcoria test by RM and ARMFA.

Table 8

Leaching concentration of heavy metal by RM, RMFA, and ARMFA (mg L^{-1})

Heavy metal	RM	RMFA	ARMFA	National standard toxicity limit
Pb	0.560	0.371	0.293	5
Cd	0	0	0	1
Cr	1.251	0.675	0.701	15
Hg	0	0	0	0.1
Zn	0.146	0.017	0.004	100

When the mass ratio of RM, FA, and water was 19:1:7 and 0.15% HPMC, 4% C_2S , 1% H_2O_2 , and 0.2% MnO_2 were added, the ARMFA was characterized by a pH of 9.25, a specific surface area of $40.54 \text{ m}^2 \text{ g}^{-1}$, a pore volume of $2.10 \text{ cm}^3 \text{ g}^{-1}$, a compressive strength of 1.31 KPa, and a soaking powdering rate of 3.72% at 24 h. When the initial total P concentration was 156.7 mg L^{-1} , the amount of ARMFA was 25 g L^{-1} , and the adsorption time was 14 h, the total P adsorption capacity could reach 38.46 mg g^{-1} , and the removal rate of P reached as high as 98.17%. The preparation process of the particle adsorbent by the nonthermal method had the advantages of being environment-friendly and inexpensive due to low energy consumption. Furthermore, the double-layer structure had significant beneficial effects on the enhancement of the adsorption capacity and strength.

The pseudo-second-order kinetic model could best describe the adsorption process of phosphorus by the ARMFA, and the adsorption process of the ARMFA was more consistent with the Langmuir model, which concerns monolayer adsorption.

In the adsorption system, when the pH was 8–9, P mainly existed in the form of HPO_4^{2-} and PO_4^{3-} , which is consistent with the existing state of phosphate in an aqueous solution as reported in the literature. These ions and positively charged $\text{Ca}^{2+}/\text{Na}^+/\text{Al}^{3+}/\text{Mg}^{2+}$ formed strong chemical bonds by precipitation, surface deposition, and ion exchange coordination and were distributed on the inner surface of the ARMFA tunnel.

Acknowledgement

This research was funded by the National Natural Science Foundation of China (U1812402, 51964010).

References

- [1] S. Habis Al-Zoubi, S. Salah Al-Thyabat, Treatment of a Jordanian phosphate mine wastewater by hybrid dissolved air flotation and nanofiltration, *Mine Water Environ.*, 31 (2012) 214–224.
- [2] State Environmental Protection Administration in China, Water and Wastewater Monitoring and Analysis Methods Committee, Water and Wastewater Monitoring and Analysis Methods, 4th ed., Environmental Science Press, China, 2002.
- [3] U. Kumari, S.K. Behera, B.C. Meikap, A novel acid-modified alumina adsorbent with enhanced defluoridation property: kinetics, isotherm study and applicability on industrial wastewater, *J. Hazard. Mater.*, 365 (2019) 868–822.
- [4] X.Q. Li, J. Cui, Y.S. Pei, Granulation of drinking water treatment residuals as applicable media for phosphorus removal, *J. Environ. Manage.*, 213 (2018) 36–46.
- [5] S. Mor, K. Chhoden, K. Ravindra, Application of agro-waste rice husk ash for the removal of phosphate from the wastewater, *J. Cleaner Prod.*, 129 (2016) 673–680.
- [6] A. Bhatnagar, V.J.P. Vilar, C.M. Botelho, R.A. Boaventura, A review of the use of red mud as adsorbent for the removal of toxic pollutants from water and wastewater, *J. Environ. Technol.*, 32 (2011) 231–249.
- [7] Y. Wang, Y. Yu, H.Y. Li, C.C. Shen, Comparison study of phosphorus adsorption on different waste solids: fly ash, red mud, and ferric-alum water treatment residues, *J. Environ. Sci.*, 50 (2016) 79–86.
- [8] R. Cai, X. Wang, X.G. Ji, B. Peng, Phosphate reclaim from simulated and real eutrophic water by magnetic biochar derived from water hyacinth, *J. Environ. Manage.*, 187 (2017) 212–219.
- [9] Y.Z. Wang, L.Y. Zhang, Y. Mo, G. Wei, Preparation of a low-cost adsorption material from red mud and bagasse, *Mater. Manuf. Processes*, 31 (2016) 162–167.
- [10] P.B. Cusack, M.G. Healy, P.C. Ryan, Enhancement of bauxite residue as a low-cost adsorbent for phosphorus in aqueous solution, using seawater and gypsum treatments, *J. Cleaner Prod.*, 179 (2018) 217–224.
- [11] V.R. Chate, R.M. Kulkarni, D.V.G. Mutaliket, B.K. Purandara, Seawater-washed activated bauxite residue for fluoride removal: waste utilization technique, *J. Environ. Sci.*, 144 (2018) 1–11.
- [12] T.F. Guo, H.Q. Yang, Q.Y. Liu, H. Gu, N. Wang, W. Yu, Y. Dai, Adsorptive removal of phosphate from aqueous solutions using different types of red mud, *Water Sci. Technol.*, 182 (2017) 570–577.
- [13] W.M. Xie, F.P. Zhou, X.L. Bi, D.D. Chen, J. Li, S.Y. Sun, J.Y. Liu, X.Q. Chen, Accelerated crystallization of magnetic 4A-zeolite synthesized from red mud for application in removal of mixed heavy metal ions, *J. Hazard. Mater.*, 358 (2018) 441–449.
- [14] A.N. Babu, G.V.K. Mohan, K. Kalpana, K. Ravindhranath, Removal of lead from water using calcium alginate beads doped with hydrazine sulphate-activated red mud as adsorbent, *J. Anal. Methods Chem.*, 12 (2017) 1–13.
- [15] S.L. Narayanan, G. Venkatesan, I.V. Potheher, Equilibrium studies on removal of lead(II) ions from aqueous solution by adsorption using modified red mud, *Int. J. Environ. Sci. Technol.*, 15 (2018) 1687–1698.
- [16] T. Le, H.R. Wang, S. Koppala, S. Ju, Q. Wang, X. Li, Pore-forming mechanism of granular red mud by microwave activation and its application in organic dyes adsorption from aqueous solution, *Mater. Res. Express*, 5 (2018) 85–101.
- [17] Z.P. Hu, Z.M. Gao, X. Liu, Z.Y. Yuan, High-surface-area activated red mud for efficient removal of methylene blue from wastewater, *Adsorpt. Sci. Technol.*, 36 (2018) 62–79.
- [18] P. Hu, Y.H. Zhang, F.Z. Lv, W.S. Tong, Preparation of layered double hydroxides using boron mud and red mud industrial

- wastes and adsorption mechanism to phosphate, *Water Environ. J.*, 31 (2016) 145–157.
- [19] R.G. Mavinkattimath, V.S. Kodialbail, S. Govindan, Simultaneous adsorption of remazol brilliant blue and disperse orange dyes on red mud and isotherms for the mixed dye system, *Environ. Sci. Pollut. Res.*, 24 (2017) 18912–18925.
- [20] G. Venkatesan, S.L. Narayanan, Synthesis of Fe₂O₃ coated and HCl-treated bauxite ore waste for the adsorption of arsenic (III) from aqueous solution: isotherm and kinetic models, *Chem. Eng. Commun.*, 205 (2017) 34–46.
- [21] N.T. do-Prado, A.P. Heitmann, H.S. Mansur, A.A. Mansur, L.C.A. Oliveira, C.S. de-Castro, PET-modified red mud as catalysts for oxidative desulfurization reactions, *J. Environ. Sci.*, 57 (2017) 312–320.
- [22] K.W. Jung, M.J. Hwang, T.U. Jeong, D.M. Chau, K. Kim, K.H. Ahn, Entrapment of powdered drinking water treatment residues in calcium-alginate beads for fluoride removal from actual industrial wastewater, *J. Ind. Eng. Chem.*, 39 (2016) 101–111.
- [23] W.Y. Wu, D.Y. Chen, J.W. Li, M.H. Su, Enhanced adsorption of uranium by modified red mud: adsorption behavior study, *Environ. Sci. Pollut. Res.*, 25 (2018) 18096–18108.
- [24] J.H. Lv, L.J. Yuan, X. Chen, L. Liu, D.C. Luo, Phosphorus metabolism and population dynamics in a biological phosphate-removal system with simultaneous anaerobic phosphate stripping, *Chemosphere*, 117 (2014) 715–721.
- [25] Y.S. Ho, G. McKay, Pseudo-second-order model for sorption processes, *Process Biochem.*, 34 (1999) 451–465.
- [26] I. Langmuir, The adsorption of gases on plane surfaces of glass mica and platinum, *J. Am. Chem. Soc.*, 40 (1916) 1361–1403.
- [27] A. Maiti, S. Das Gupta, J.K. Basu, S. De, Adsorption of arsenite using natural laterite as adsorbent, *Sep. Purif. Technol.*, 55 (2007) 350–359.
- [28] S.Y. Yoon, C.G. Lee, J.A. Park, J.H. Kim, S.B. Kim, S.H. Lee, J.W. Choi, Kinetic equilibrium and thermodynamic studies for phosphate adsorption to magnetic iron oxide nanoparticles, *Chem. Eng. J.*, 236 (2014) 341–347.
- [29] J. Jang, D.S. Lee, Effective phosphorus removal using chitosan/Ca-organically modified montmorillonite beads in batch and fixed-bed column studies, *J. Hazard. Mater.*, 375 (2019) 9–18.
- [30] C. Han, Z. Wang, W.J. Yang, Q. Wu, H. Yang, X. Xue, Effects of pH on phosphorus removal capacities of basic oxygen furnace slag, *Ecol. Eng.*, 89 (2016) 1–6.
- [31] S. Ding, D.X. Fang, Z.S. Pang, B. Luo, L. Kuang, H. Wang, Q. Zhang, Q. Shen, F. Ji, Immobilization of powdery calcium silicate hydrate via PVA covalent cross-linking process for phosphorus removal, *Sci. Total Environ.*, 645 (2018) 937–945.
- [32] D. Wang, N. Chen, Y. Yu, W. Hu, C. Feng, Investigation on the adsorption of phosphorus by Fe-loaded ceramic adsorbent, *J. Colloid Interface Sci.*, 464 (2016) 277–284.
- [33] L.Q. Wang, Removal of Phosphate from Wastewater by Bitten-Heat Treated Red Mud, Guangxi University, China, 2013.
- [34] Y.Q. Zhao, Preparation and Characterization of a Novel Red Mud Granular Adsorbent for Phosphate Removal, Shandong University, China, 2013.